PHOTOMASK

BACUS—The international technical group of SPIE dedicated to the advancement of photomask technology.

BACUS N • E • W • S

SEPTEMBER 2019
VOLUME 35, ISSUE 9

Photronics Best Student Oral Finalist

EUV Mask Characterization with Actinic Scatterometry

Stuart Sherwin and Andrew Neureuther, University of California Berkeley, Department of Electrical Engineering and Computer Science, Berkeley, USA

Patrick Naulleau, Center for X-Ray Optics, Lawrence Berkeley National Laboratory, Berkeley, USA

Abstract

With EUV Lithography rapidly approaching maturity, accurate metrology to thoroughly characterize EUV photomasks is needed. We present an actinic EUV reflection-based scatterometry technique to measure key parameters of EUV photomasks to characterize both the multilayer mirror substrate as well as periodic absorber targets fabricated on the multilayer. We show these measurements can be used both in determining the physical dimensions on the mask, and also in directly quantifying optical effects, which can provide invaluable feedback in the mask optimization and manufacturing processes. In this paper, we present four different methods of data analysis for EUV mask scatterometry: two for characterizing the multilayer mirror based on measurements of the reflected light intensity from a flat open area of the mask, and two more for characterizing absorber gratings fabricated on the multilayer substrate based on measurements of the diffraction efficiencies. Key findings include that a simple neural net architecture containing a single fully connected hidden layer that can characterize the multilayer's angularly-varying complex reflection coefficient to 7×10^{-4} accuracy, and that dictionary-based scatterometry with 7 wavelengths from 13.2 – 13.8nm can measure the absorber thickness of a grating to 0.4nm even in the presence of random and systematic errors. With the presented methods and findings, we hope to demonstrate that actinic EUV scatterometry has the capabilities to accurately characterize EUV masks in terms of both multilayer and absorber.

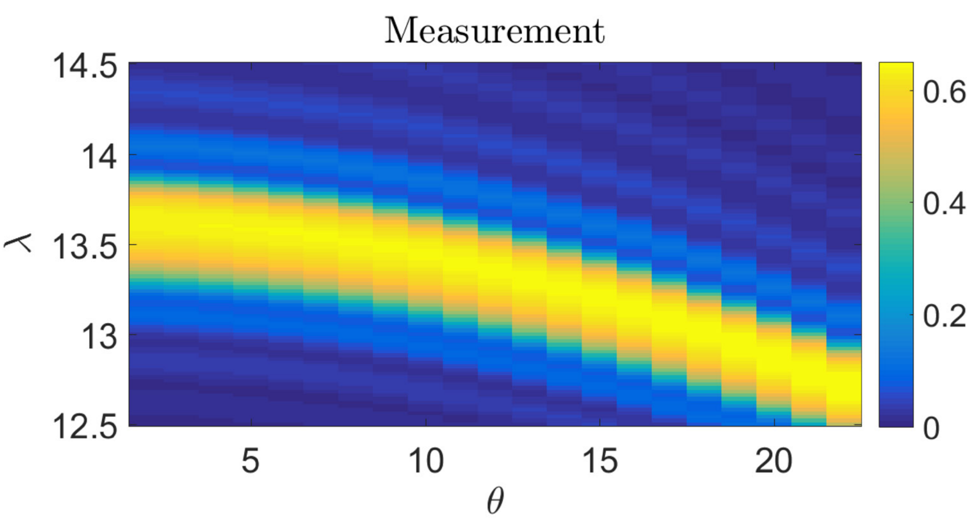

Figure 1. Measured reflected intensity from MoSi multilayer mirror as a function of wavelength [nm] and angle [degrees].

Take A Look Inside:

SPIE.

10809-27

EDITORIAL

The Next Evolution of Merchant Mask Makers: Partnerships to Scale

Bryan Kasprowicz, Photronics, Inc.

For many years, the trend in the semiconductor industry regarding photomasks and chipmakers was to shed captive mask operations in favor of merchant photomask suppliers. Over the course of the last decade, however, a converse trend has emerged as leading-edge production technology has become ever more complex and costly. Captive mask shops have become a competitive necessity among first-tier device makers, which tend to be more vertically integrated.

It is the capital-intensive nature of manufacturing at the leading edge, perhaps more than any other factor, that has caused the reversal of captive and merchant mask trends. But coupled with this is the changing nature of end markets, namely an increasing reliance on vast consumer devices, which puts pressure on development and manufacturing cycle times.

These end markets are driving the semiconductor Industry to trend towards a bifurcated roadmap where technology is seen as mature or pervasive (from a midrange ~45nm to ~22nm to a low-end of ~90nm and above) and leading-edge or advanced (~14nm and below). Each of these technologies has their own priorities that must be accounted for by the mask maker. In the mature case, customers are looking to differentiate their products, extend fab lifetimes and add capacity. This technology leverages existing mask infrastructure where limited investments are required to support, save for adding capacity to meet the demand (which is very difficult as Tom Faure pointed out in his editorial for the BACUS Newsletter in August 2019 titled "Mask Maker Appreciation.") The leading-edge case has a more traditional roadmap where Processes-of-Record (POR's) are being established jointly with the customer during development, or by integrating into an established POR that requires close partnership to meet leading edge targets and drives development learning cycles. Certainly, the easier path in this technology is to be the established POR, however, there is much to gain from integration. In either case, the barrier to entry and continued support of these nodes are quite high for merchant mask makers, often echoing the significant investments of the captive ones.

At first glance, it might seem there is a dwindling place for merchant photomask makers at the leading edge, given the cost involved and the competitive benefits a captive mask operation provides. But this isn't really the case; the larger merchant mask makers aren't likely to leave the market anytime soon, but they may look to each other to find their way.

As the merchant mask makers continue to evolve and redefine their role, to maximize their development efforts and investments, economies of scale are necessary. In order to accomplish this in a meaningful way, partnerships with suppliers, competitors, and customers alike are being formed; helping to further evolve the ecosystem required to enable advanced patterning. In this way, we can leverage the expertise in each of these areas. We can help bring fast convergence on several challenges from EDA and materials with suppliers to additional know-how, IP and scale with competitors*. Lastly, customers, including captives, are pulling harder to build long term strategic partnerships across all technology nodes to drive learning cycles, identify challenges and develop solutions. Chris Progler showcased these benefits at SPIE Advanced Lithography in March 2019 in a joint paper with IBM titled "EUV mask challenges and requirements for ultimate single exposure interconnects."

On both sides of the roadmap, more technology is being pushed to the mask makers. They continue to evolve and support, from design enablement to driving the ecosystem, to improving time to yield, to investments to allow for tomorrow's needs. Masks are at the center of the critical design to manufacturing handoff point and are moving or have moved outside of the commodity realm and into a key enabler role. A role we have accepted with aplomb.

As a last-minute reminder - much of the recent technical advancements by mask makers and their ecosystem will be on display at the annual Photomask Technology and EUVL Symposium (September 15-19), hope to see you there.

* Photronics and DNP changed the merchant mask landscape through such partnerships in Taiwan and China.

BACUS

N • E • W • S

BACUS News is published monthly by SPIE for *BACUS*, the international technical group of SPIE dedicated to the advancement of photomask technology.

Managing Editor/Graphics Linda DeLano

SPIE Sales Representative, Exhibitions, and Sponsorships Melissa Farlow

BACUS Technical Group Manager Marilyn Gorsuch

SPIE.

P.O. Box 10, Bellingham, WA 98227-0010 USA
Tel: +1 360 676 3290
Fax: +1 360 647 1445
SPIE.org
help@spie.org

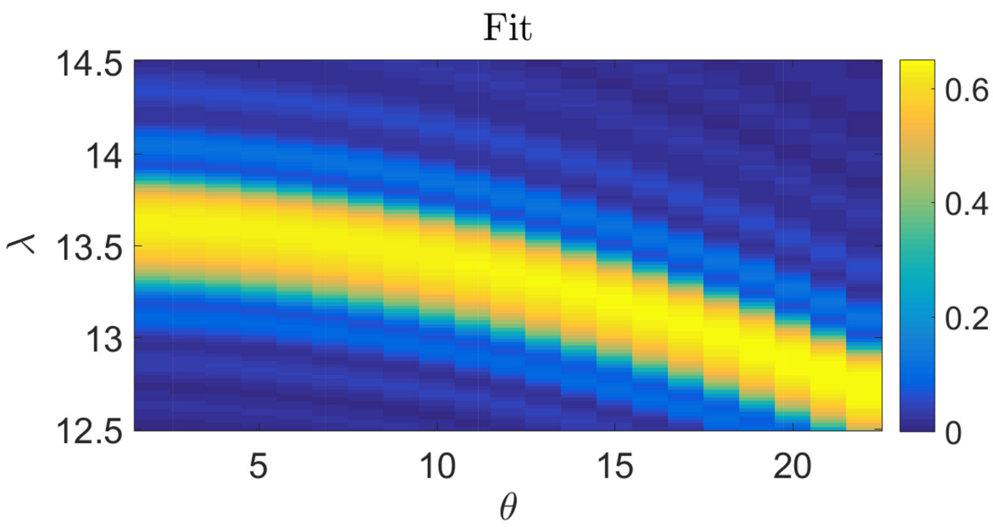

Figure 2. Modeled reflected intensity from Fresnel reflection coefficient of fitted multilayer model.

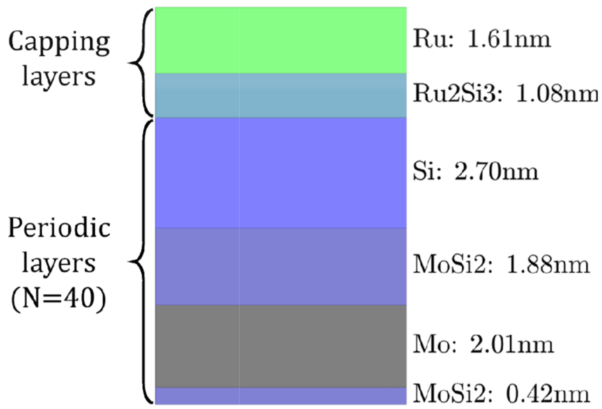

Figure 3. Fitted thicknesses in multilayer stack.

1. Introduction

Actinic metrology is of critical importance for EUV photomasks, due to the lithographic sensitivity to both amplitude and phase effects, which can only be directly probed at the wavelength in question, namely 13.5nm. However, due to challenges with regard to the cost, complexity, and efficiency of EUV optics, it is highly desirable to use the simplest hardware possible. Scatterometry employs simpler hardware than imaging in that it does not require imaging optics—only illumination optics to strike an area on the mask with a plane wave, and a sensor some distance from the mask to measure the diffraction pattern. This is strictly simpler than an imaging system, which would still require illumination optics and a similar sensor, but would also require imaging optics, and would furthermore be sensitive to aberrations, unlike scatterometry. So, from a hardware perspective there are clear advantages to actinic EUV scatterometry over imaging; the key question we attempt to address here is whether scatterometry contains the relevant information to characterize EUV photomasks.

In addressing this question, we explore two different types of models, both of which can be employed to interpret the raw scatterometry data. First, we consider parametric models, models which explicitly consider the physical geometry and material properties. We assume certain material properties and approximate geometries, and then via rigorous physical calculations such as the Fresnel reflection coefficient or Rigorous Coupled-Wave Analysis (RCWA), we attempt to find the geometrical dimensions that best explain the data. This leads to a clear physical interpretation and a high degree of accuracy—if the underlying model is sufficiently accurate. Indeed, these benefits come with a *caveat* that if assumptions of the model are violated, the results may be seriously corrupted. The second type of model is what we refer to as nonparametric models. This approach provides a purely optical (rather than geometrical and material) description of the mask. This can be seen as a drawback if the goal is to measure the physical dimensions of structures on the mask; however, if the goal is to predict the imaging performance of a mask, an optical description would be precisely what is desired. These approaches also come with the benefit that one does not need to have as much prior knowledge of the 3D geometry and material properties on the mask; in this sense, they are much more flexible than parametric approaches.

In section 2, we discuss the problem of characterizing the multilayer mirror substrate, utilizing parametric and nonpara-

Table 1. Ranges of parameters for generating randomized multilayer designs.

Parameter	Min	Max
d [nm]	6.9	7
gamma	0.35	0.45
MoSi2 A [nm]	0	1.5
MoSi2 B [nm]	0	1.5
Ru [nm]	1	3
Ru2Si3 [nm]	0	2
attenuation	0.95	1

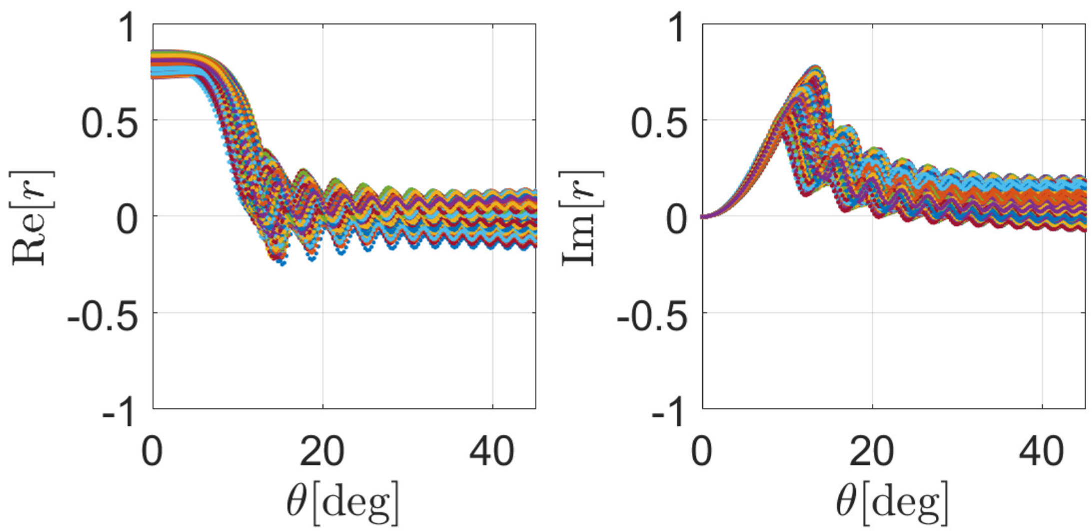

Figure 4. Output training data for all 10^4 randomly generated multilayers.

metric approaches. Section 2.1 describes parametrically fitting the thicknesses of layers in the multilayer stack using nonlinear least-squares; we show good agreement with experimentally measured reflectivity data using this approach, although we do not have a way to independently verify the correctness of the fit. Section 2.2 describes the nonparametric approach of feeding measured intensity *vs* angle into a trained neural network, which returns the complex reflection function directly; we show the performance of this method in a simulation with randomly generated multilayer designs and observe a high degree of accuracy. In section 3, we discuss the problem of characterizing an absorber grating fabricated on top of the previously characterized multilayer mirror substrate, again utilizing parametric and nonparametric approaches. Section 3.1 describes the parametric approach of fitting the duty cycle and thickness of the absorber grating from the measured diffraction efficiencies using a dictionary-based method; we demonstrate the robustness of this approach and quantify tolerances to certain random and systematic errors by means of Monte-Carlo simulation. Section 3.2 describes the nonparametric approach of solving for an arbitrary duty cycle and complex transmission coefficient of the absorber. In total, these four methods represent parametric and nonparametric methods to characterize both the multilayer and absorber on EUV masks.

2. Multilayer Characterization

In this section, we discuss the problem of characterizing the multilayer mirror substrate of an EUV photomask from measurements of the reflected intensity as a function of wavelength and/or angle of illumination. These measurements could either be made on a large open area of the mask, or on the multilayer blank before absorber deposition. We first discuss a parametric method to retrieve the thicknesses of layers in the multilayer stack, and second discuss a nonparametric method to directly retrieve the complex reflection coefficient *vs* angle.

2.1 Parametric multilayer characterization

The parametric method of retrieving the thicknesses of layers in the multilayer stack has been previously presented[1] but is briefly summarized here for completeness. Our multilayer mirror nominally consists of 40 periodic Mo-Si layers with an Ru capping layer; however, following Chao[2], we additionally include interdiffusion layers of Ru2Si3 at the Ru-Si interface, and MoSi2 at every Mo-Si interface. Additionally, the thickness of the MoSi2 is allowed to be different at the Mo-on-Si and Si-on-Mo interfaces. For all materials, we assume the nominal complex indices of refraction given by the CXRO database[3].

Fig. 1 shows the experimentally measured reflectivity data from an open area on a multilayer mirror; measurements were taken at the Advanced Light Source Reflectometry and Scattering Beamline (6.3.2). We adjust the thicknesses of layers in our

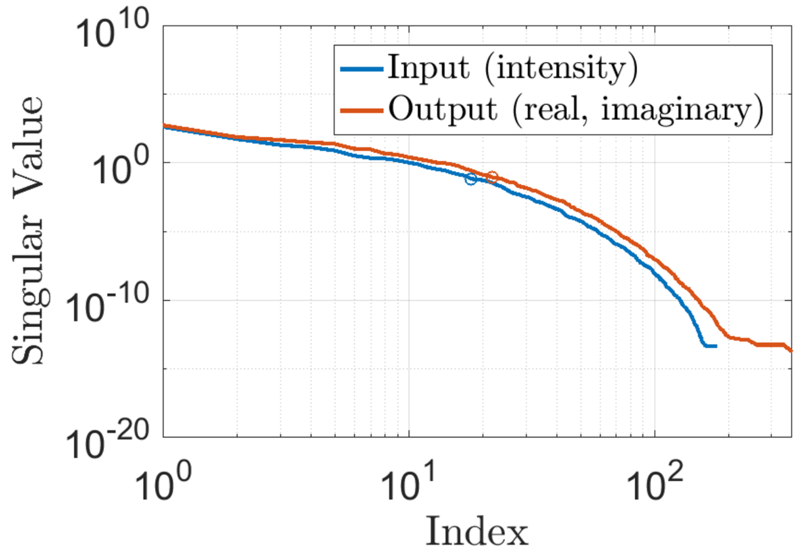

Figure 5. Singular value decay for input and output data.

fit to minimize the squared error between this measurement and the reflectivity calculated via the Fresnel reflection coefficient. Fig. 2 shows the recovered reflectivity from the fitted multilayer stack, which exhibits very good qualitative and quantitative (RMSE=1.3%) agreement with the measured data. Fig. 3 shows the recovered multilayer stack.

We note that, while the fit agrees quite well with the measured reflectivity, it is difficult to quantify the accuracy of the recovered thicknesses, because it is possible that the complex indices of refraction deviate from their nominal value, or that the layers are not perfectly periodic, etc. These difficulties in creating an appropriate physical model motivate the need for next section.

2.2 Nonparametric multilayer characterization

In this section, we sidestep the problem of recovering the exact physical dimensions of the multilayer stack, by raining a neural network to directly output the multilayer's complex reflection coefficient *vs* angle given a measurement of the reflected intensity *vs* angle. We generate a set of coefficient *vs* angle given a measurement of the reflected intensity *vs* angle. We generate a set of 10^4 random multilayer designs consisting of the same basic architecture as shown in Fig. 3, but with thicknesses chosen uniformly at random according to the ranges shown in Table 1. For each multilayer stack, we evaluate the Fresnel reflection coefficient at angles ranging from 0-45 degrees in steps of 0.25 degrees. Now we take the modulus-squared of the reflection coefficients to represent measured intensity *vs* angle; our task is from this data to deduce the real and imaginary parts of the reflection coefficient *vs* angle. To avoid phase ambiguity, we fix the phase at 0 degrees to be 0; the real and imaginary parts of the entire data set, with phase normalized in this way, are shown in Fig. 4.

Define $m \stackrel{\text{def}}{=} 181$ (the number of measured angles) and $n \stackrel{\text{def}}{=} 10^4$ (the number of randomly generated multilayer designs). For multilayer stack index *i*, denote the complex reflectivity (with normalized phase) at the sampled angles as $\mathbf{r_i} \in \mathbb{C}^m$; define the intensity vector to be $\mathbf{x_i} \stackrel{\text{def}}{=} |\mathbf{r_i}|^2 \in \mathbb{R}^m$ (where the absolute-value-squared operation is carried out element-wise); and define the real-imaginary parts vector to be $\mathbf{y_i} \stackrel{\text{def}}{=} [\mathrm{Re}[\mathbf{r_i}]; \mathrm{Im}[\mathbf{r_i}]] \in \mathbb{R}^{2m}$. We desire a function $f: \mathbb{R}^m \to \mathbb{R}^{2m}$, which maps intensity vectors to real-imaginary parts vectors. The core of this function will be a fully connected neural network, but to simplify the training process we first reduce the dimensionality of both the input and output data via the truncated SVD (singular value decomposition). The process is described in detail only for input vectors, as the process for output vectors is virtually identical. Define the matrix $\mathbf{A} = [\mathbf{x_1}| \ldots |\mathbf{x_n}] \in \mathbb{R}^{m \times n}$, and let $\mathbf{A} = \mathbf{USV^T}$ be its (compressed) SVD, where $\mathbf{U} \in \mathbb{R}^{m \times n}$ and $\mathbf{V} \in \mathbb{R}^{m \times m}$ have orthonormal columns and $\mathbf{S} \in \mathbb{R}^{m \times m}$ is diagonal with nonnegative entries. The most accurate rank-*k* approximation to $\mathbf{A}$ (with respect to the Frobenius norm) is given by the truncated SVD[4]—namely $\mathbf{A_k} = \mathbf{U_k S_k V_k^T}$, where $\mathbf{U_k}$ and $\mathbf{V_k}$ consist of the first *k* columns of $\mathbf{U}$ and $\mathbf{V}$, respectively, and $\mathbf{S_k}$ is a diagonal matrix consisting of the first *k* rows and columns of $\mathbf{S}$. From this decomposition, $\mathbf{U_k}$ provides an efficient *k*-dimensional basis to represent the $\mathbf{x_i}$ vectors; therefore, we represent each vector by its *k* coefficients in this basis: $\mathbf{c_i^x} = \mathbf{U_k^T x_i}$. Following a similar process for the $\mathbf{y_i}$ vectors, we obtain a lower-dimensional representation $\mathbf{c_i^y}$. Due to the rapid decay of singular values in both $\mathbf{x_i}$ and $\mathbf{y_i}$ (Fig. 5), a significant reduction of dimension is possible without introducing much error: for the input, the dimension was reduced from 181 to 18 (90% reduction), and for the output the dimension was reduced from 362 to 22 (94% reduction).

After this dimensionality reduction, we train a neural network to map the input coefficients ($\mathbf{c_i^x}$) to the output coefficients ($\mathbf{c_i^y}$). The network is implemented using the MATLAB Neural Network Toolbox; the network architecture is shown in Fig. 6, and consists of an 18-dimensional input, one fully connected hidden layer with 50 units, and a 22-unit output layer. The network is trained with the 10^4 multilayer examples, using a 70-15-15 split between training, testing, and validation data. Fig. 7 shows the performance of the trained network on each of these datasets, where we see approximately 7×10^{-4} RMSE on the testing data, and only slightly better performance on the training data. The relatively small difference between training and testing performance is a positive sign that the network is not overfitting the data. Fig. 8 shows the worst-case performance from the testing dataset, where we see a high level of qualitative accuracy, suggesting that this method can be an attractive alternative to the parametric approach.

3. Absorber Characterization

In this section we discuss the problem of characterizing an absorber grating fabricated on top of a previously characterized multilayer mirror. Again, we consider both parametric and a nonparametric approach. In section 3.1 we consider recovering the duty cycle and thickness of the TaN absorber using measurements of the diffraction pattern *vs* wavelength; the

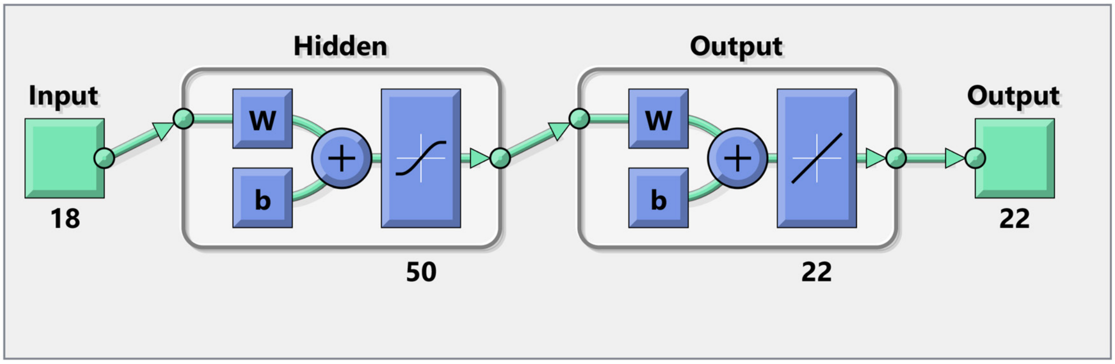

Figure 6. Neural network architecture. From left to right: Input 18 singular value coefficients for intensity, passed to one fully connected hidden layer with 50 units, passed to the 22-unit output layer, which returns 22 singular value coefficients representing the real and imaginary parts of the reflection coefficient.

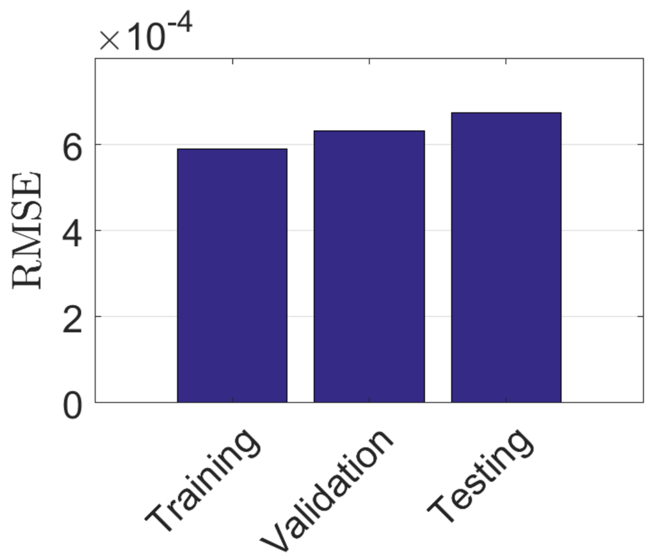

Figure 7. RMSE in training, validation, and test sets. Note that the error is only slightly better in the training set, implying that we have largely avoided overfitting the data.

multilayer must be previously characterized using the parametric method. In section 3.2 we consider recovering the duty cycle and absorber amplitude and phase from measurements of the diffraction pattern *vs* illumination angle; the multilayer must be previously characterized by either the parametric or nonparametric method in this case.

3.1 Parametric absorber characterization

The first approach we describe for characterizing a grating on a multilayer mirror is based on a dictionary of simulated diffraction measurements for different grating designs. We vary the duty cycle (D) and thickness (t) of a TaN grating on top of the multilayer shown in Fig. 3, and run RCWA (Rigorous Coupled-Wave Analysis) for each grating design. Each grating design requires multiple instances of RCWA to simulate varying the wavelength or illumination angle. In this case, we chose a dictionary for a nominal grating design of mask pitch p = 400nm, D = 0.5, t = 80nm, with pure TaN absorber and 90° sidewall angle (SWA). The dictionary consists of 11 diffraction orders (−5: 5), 7 wavelengths (λ = 13.2: 0.1: 13.8 nm), 41 values of duty cycle (D = 0.4: 0.005: 0.6), and 61 values of thickness (t = 65: 0.5: 95 nm); this dictionary is shown in Fig. 9. We also tested a dictionary with the same ranges of D and t, but only a single wavelength (λ= 13.5 nm). Time to generate a dictionary is linear in the number of RCWA runs required, although the different runs could clearly be done in parallel if runtime were a major concern. For the 7-wavelength dictionary, 17,507 RCWA runs were required, taking approximately 5 hours. Also note that this is a one-time setup cost to generate the library, and the time to process a measurement once the dictionary has been created is much shorter. All RCWA runs were conducted by calling the Panoramic EM-Suite API from MATLAB.

To test the performance of the dictionary, we simulated scatterometry measurements for gratings of random design in the vicinity of the nominal design, with varying levels of random and systematic errors or perturbations. The random errors consist of multiplicative noise, and the systematic errors consist of perturbations to the sidewall angle (SWA) or the optical density. Scatterometry measurements for each of these designs were simulated with varying levels of perturbation strength and noise; then, each simulated diffraction signal was compared to

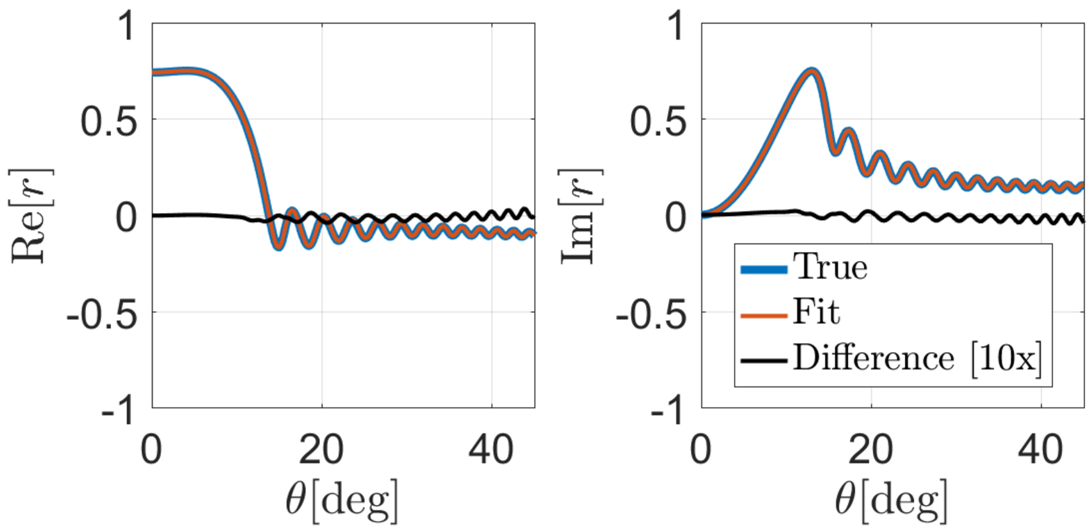

Figure 8. Worst-case fit. Note that even in the worst case, the neural network attains very good performance.

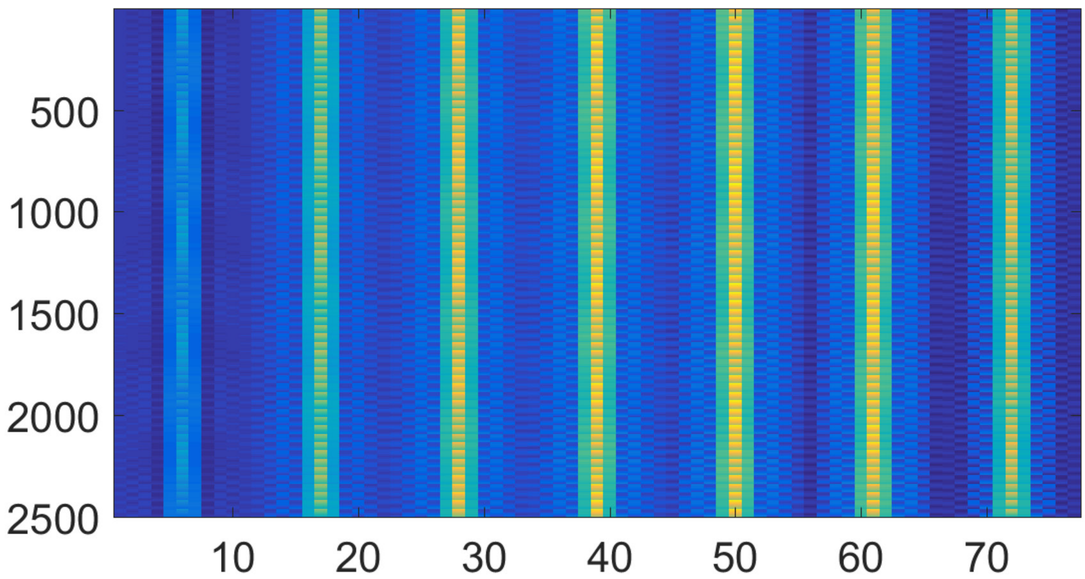

Figure 9. Dictionary for measuring (D, t) from measurements of 11 diffraction orders at 7 wavelengths. Rows are combinations of (D, t), and columns are combinations of diffraction order and wavelength.

the dictionary, and the element closest to the measurement in the Euclidean sense was reported as the fitted (D, t); for greater accuracy, we also performed linear interpolation between dictionary elements. The main limitation on the performance appears to arise from periodic local minima in the cost function *vs* thickness (Fig. 10), which occur at a period of approximately $\Delta t = \frac{\lambda}{2cos\theta}$; this period suggests that the source of these periodic minima is the interference between the background and the reflection from the top of the absorber (Fig. 11). This interference is closely related to the absorber "swing curve"[5,6].

In the absence of random and systematic errors, the true solution will always be the global minimum, so the spurious local minima are not a major concern. However, either random or systematic errors of sufficient magnitude can lead a spurious local minimum to become the global minimum of the cost function, resulting in an unacceptably large thickness error on the order of $\frac{\lambda}{2}$.

The rate of these errors as a function of SWA is shown in Fig. 12. Note that the 7-wavelength dictionary is far more robust to these errors than the single-wavelength dictionary. From this result, we can tolerate approximately 4° of SWA mismatch between the dictionary and the true absorber profile without resulting in serious errors. We define the error tolerance as the maximum level at which none of the 100 random mask designs led to a thickness error > $\frac{\lambda}{4}$. Tolerances to random and systematic errors are summarized in Table 2; note that the random error tolerance is 0.4%, which is within the stated accuracy of the beamline, 0.08%[7]. The RMSE at the maximum level of random and systematic errors is reported in Table 2. Note that

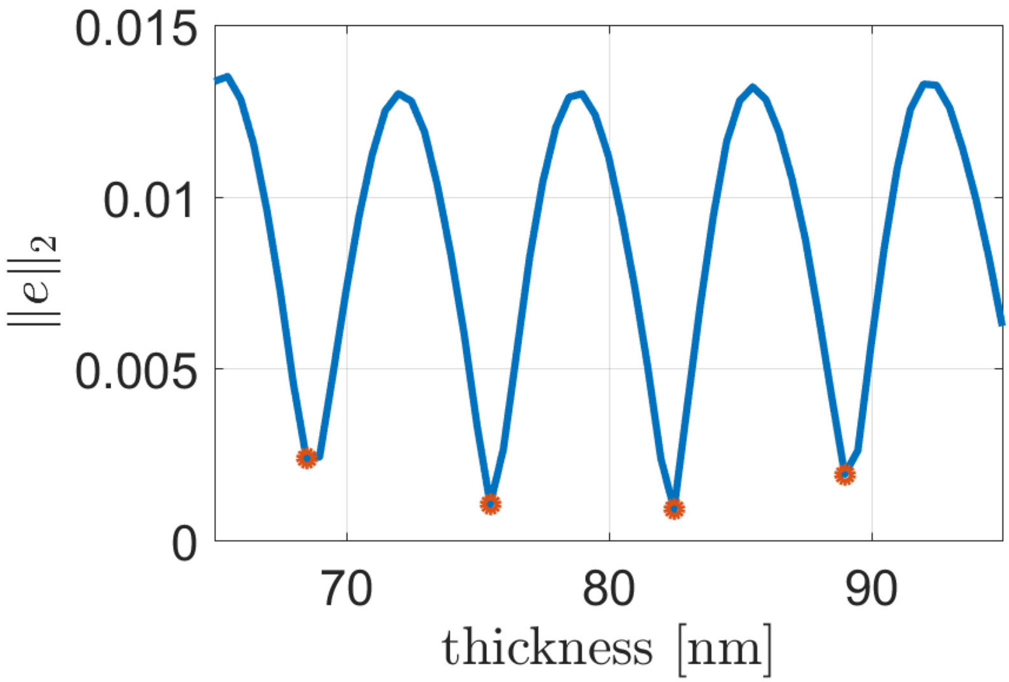

Figure 10. Demonstration of periodic local minima vs thickness.

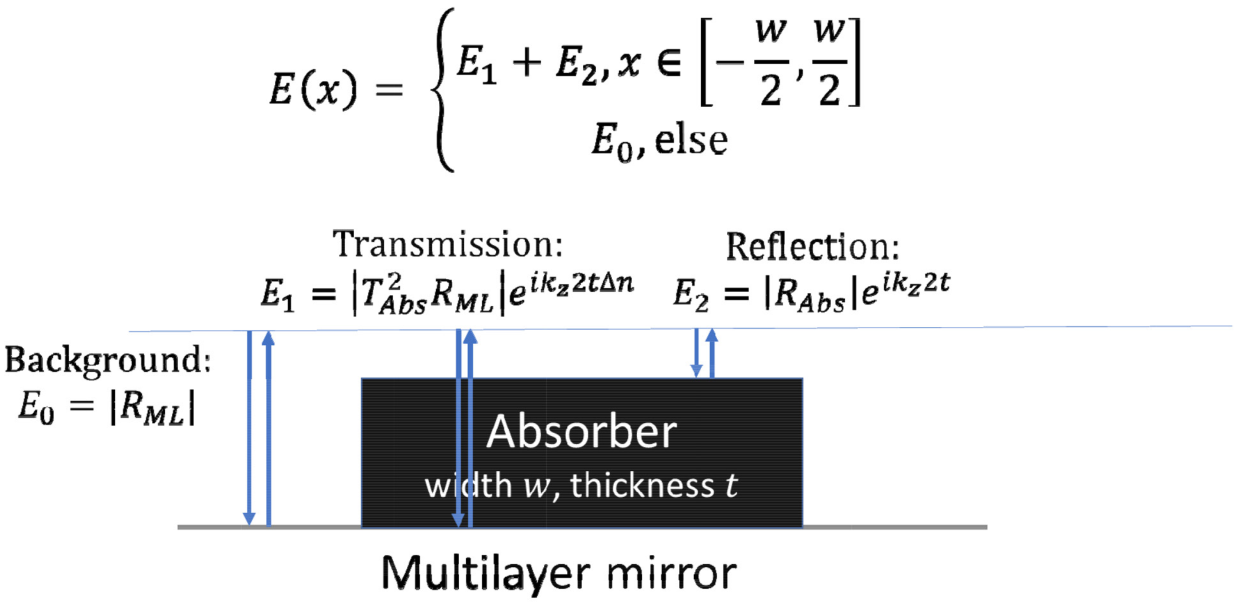

Figure 11. Spurious local minima can be explained by a Fresnel-Kirchhoff model as the result of interference between the background and the reflection from the top surface of the absorber.

both metrics can likely be improved by measuring additional wavelengths and/or angles.

3.2 Nonparametric absorber characterization

A mathematical model to describe the reflected diffraction pattern from an EUV mask has been described by the authors of this paper[1], and an essentially equivalent model has also been previously proposed by Clifford[8]. These approaches model the scattering process as downward transmission through the absorber pattern, then reflection by the multilayer according to the angularly varying multilayer reflection function, followed by upward transmission of each reflected diffraction order through the absorber pattern, and finally linear recombination of the diffraction orders with the same propagation angle.

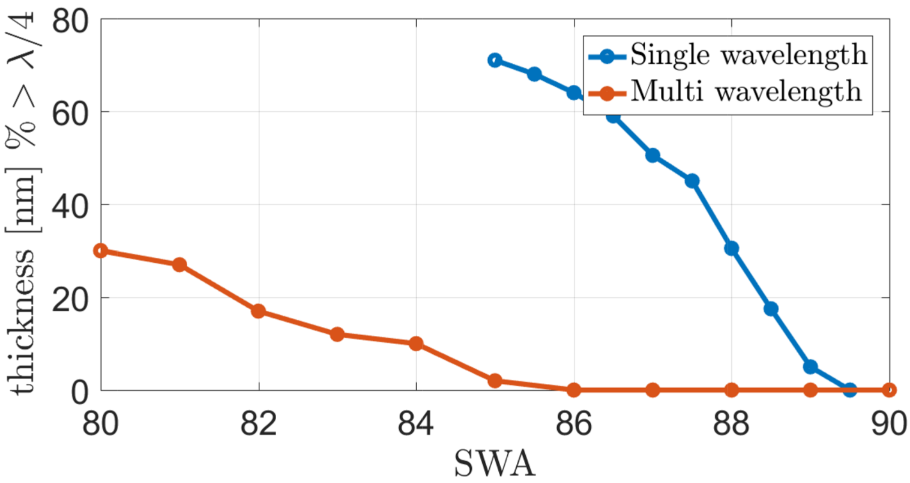

Figure 12. Comparison of single-wavelength and 7-wavelength measurement schemes. Note that the 7-wavelength method is much more robust to systematic errors in the sidewall angle.

Table 2. Error tolerances and parameter rmse for the 7-wavelength dictionary.

Error Type	Tolerance		Parameter	RMSE
SWA	4^o		D	0.07%
Optical Density	2%		t	0.4nm
Noise	0.4%			

For illumination angle θ_o, let us define the diffraction angles as $\theta_i = \sin^{-1}\left(\sin\theta_0 + i\frac{\lambda}{p}\right), i = -N, \dots, N$ and corresponding spatial frequencies $f_i = \frac{i}{p}$.

Define the complex frequency-space transmission through the patterned absorber layer from illumination angle θ as $\tilde{t}(f;\theta)$; similarly define the final complex frequency-space reflection as $\tilde{r}(f;\theta)$; finally, define the angularly varying multilayer reflection function as $r_{ML}(\theta)$. Denote the transmission diffraction vector for illumination angle θ as $\tilde{\mathbf{t}}(\theta) = [\tilde{t}(f_{-N};\theta), \dots, \tilde{t}(f_N;\theta)]^T$; similarly denote the reflection diffraction vector as $\tilde{\mathbf{r}}(\theta) = [\tilde{r}(f_{-N};\theta), \dots, \tilde{r}(f_N;\theta)]^T$; finally, define the shift operator S_i to shift the elements of a vector up by *i* rows and fill in any missing entries with zeros.

Then the reflection is (approximately) given by:

$$\tilde{\mathbf{r}}(\theta_0) \approx \sum_{i=-N}^{N} \mathcal{S}_i[\tilde{\mathbf{t}}(\theta_i)][\tilde{t}(f_i;\theta_0) r_{ML}(\theta_i)] = \left[\mathcal{S}_{-N}[\tilde{\mathbf{t}}(\theta_{-N})] | \dots | \mathcal{S}_N[\tilde{\mathbf{t}}(\theta_N)]\right] \left(\tilde{\mathbf{k}}(\theta_0) .* \tilde{\mathbf{t}}(\theta_0)\right),$$

where $\tilde{\mathbf{k}}(\theta_o) \stackrel{\text{def}}{=} [r_{ML}(\theta_{-N}), \dots, r_{ML}(\theta_N)]^T$, and .* denotes element-wise multiplication. In this paper, we make a further simplification to the model, where we assume that the transmission function of the absorber does not vary with angle over the relevant range of angles. Following this simplification, we redefine $\tilde{\mathbf{t}} = [\tilde{t}(f_{-N}), \dots, \tilde{t}(f_N)]^T$. We can now formulate our simplified, convolutional, model:

$$\tilde{\mathbf{r}}(\theta_0) \approx \mathcal{F}\left[\mathcal{F}^{-1}(\tilde{\mathbf{t}}) .* \mathcal{F}^{-1}\left(\tilde{\mathbf{k}}(\theta_0) .* \tilde{\mathbf{t}}\right)\right],$$

where F and F^{-1} respectively denote the discrete Fourier transform and its inverse. The main advantage of this model is that now we have only one unknown quantity ($\tilde{\mathbf{t}}$), rather than a separate transmission function for each illumination angle. We then take measurements of $|\tilde{\mathbf{r}}(\theta)|$ for a range of illumination angles θ, and use amplitude-based nonlinear least-squares[9] to recover the unknown vector $\tilde{\mathbf{t}}$. Note that this relies on already having previously characterized the complex multilayer reflectivity $r_{ml}(\theta)$, which allows us to accurately predict how $\tilde{\mathbf{k}}(\theta)$ changes as a function of illumination angle. Further, note that while we could in principle solve for each element of $\tilde{t}$ (i.e. solve for an arbitrary transmission function), due to the relatively simple rectangular absorber geometry, we parametrize $\tilde{\mathbf{t}}$ as the Fourier transform of a square-wave with one region of unit amplitude (vacuum), and another region of arbitrary amplitude and phase (absorber). Thus ultimately, we fit to the amplitude, phase, and duty cycle of the absorber.

We evaluated the technique by simulating scatterometry measurements from the grating on multilayer using RCWA, with illumination in the shadowing orientation at 39 angles linearly spaced from 1.6° to 9.1°; we used these diffraction amplitudes to fit the absorber parameters. To assess the accuracy of the recovered absorber transmission, we also simulated the transmission through 21the absorber in vacuum, again using RCWA. Figs. 13 and 14 show the comparison of our recovered $\tilde{\mathbf{t}}$ and $\tilde{\mathbf{r}}$ to the ground-truth RCWA, for a mask-pitch of 785nm (98nm wafer-pitch) in the shadowing orientation. Units are in wafer scale assuming 8x demagnification, as would be used in a 0.55 NA anamorphic EUV scanner. The results are encouraging qualitatively, but more work on the quantitative accuracy is still needed. Note that the main area of disagreement is the absorber region, which may suggest that the backscatter from the absorber needs to be included in the fit.

5. Conclusion

In this paper, we have discussed four methods of data analysis for actinic EUV scatterometry, demonstrating the versatile capabilities of this technique to characterize both the multilayer and absorber of EUV masks at the relevant wavelength. First, we

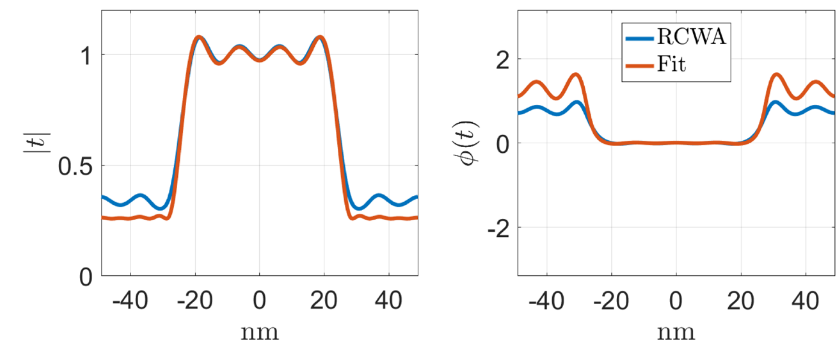

Figure 13. Fitted transmission function vs RCWA.

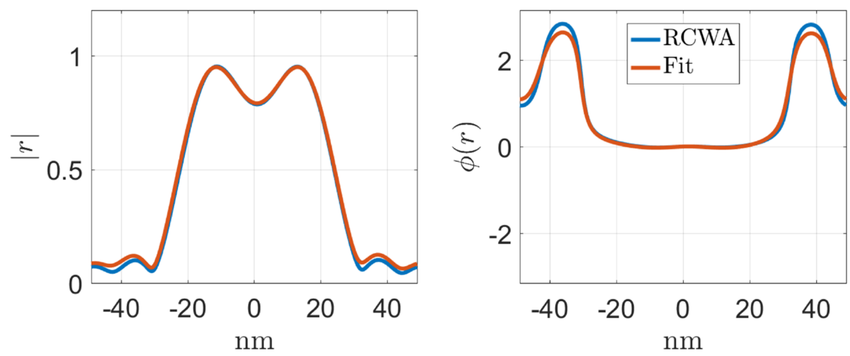

Figure 14. Fitted reflection function vs RCWA.

demonstrated parametric fitting of the thicknesses of layers in a multilayer mirror, which achieved good qualitative and quantitative agreement with the experimentally measured reflectivity data. Second, we demonstrated a nonparametric method to characterize the multilayer by training a neural network to map intensity *vs* angle to complex reflection coefficient *vs* angle; the neural net training was simplified by compressing both the input and output data using the truncated SVD, and the network itself consisted of a simple architecture with a single fully-connected hidden layer, leading to a final testing error of 7×10^{-4} RMSE. Third, we demonstrated a dictionary-based method to measure the duty cycle and thickness of an absorber grating fabricated on a (known) multilayer mirror substrate. We used Monte-Carlo simulation to explore the tolerance of the method to both random errors (up to ≤ 0.4% multiplicative noise) and systematic errors (≤ 4% sidewall angle, ≤ 2% optical density), and quantified the precision (duty cycle: 0.07%, thickness: 0.4nm). Finally, we introduced a nonparametric approach for modeling the absorber grating with an arbitrary amplitude, phase, and duty cycle; we showed qualitatively promising initial results, but further work is still required to improve the quantitative performance. Taken together, these results suggest that by fusing simple hardware (relative to imaging) with advanced computational capabilities, actinic EUV scatterometry can indeed be used to characterize EUV masks in terms of both the multilayer mirror substrate and the patterned absorber at the wavelength of interest.

Works Cited

1. S. Sherwin, A. Neureuther, and P. Naulleau. "Actinic EUV scatterometry for parametric mask quantification." Extreme Ultraviolet (EUV) Lithography IX. Vol. 10583. International Society for Optics and Photonics, 2018.
2. R. Chao, et al. "Experimental verification of EUV mask limitations at high numerical apertures." Extreme Ultraviolet (EUV) Lithography IV. Vol. 8679. International Society for Optics and Photonics, 2013.
3. B. L. Henke, E. M. Gullikson, and J. C. Davis, "X-ray interactions: photoabsorption, scattering, transmission, and reflection at e= 50-30,000 ev, z= 1-92," Atomic data and nuclear data tables 54(2), pp. 181–342, 1993.
4. L. N. Trefethen, and D. Bau III. Numerical Linear Algebra. Vol. 50. Siam, 1997.
5. E. van Setten, et al. "EUV mask stack optimization for enhanced imaging performance." Photomask Technology 2010. Vol. 7823. International Society for Optics and Photonics, 2010.
6. N. Davydova, et al. "Imaging performance improvements by EUV mask stack optimization." 27th European Mask and Lithography Conference. Vol. 7985. International Society for Optics and Photonics, 2011.
7. E. M. Gullikson, S. Mrowka, and B. B. Kaufmann, "Recent developments in euv reflectometry at the advanced light source," in Emerging Lithographic Technologies V, 4343, pp. 363–374, International Society for Optics and Photonics, 2001.
8. C. H. Clifford. Simulation and compensation methods for EUV lithography masks with buried defects. Doctoral dissertation, UC Berkeley, 2010.
9. L. H. Yeh, et al. "Experimental robustness of Fourier ptychography phase retrieval algorithms." Optics Express 23.26 (2015): 33214-33240.

BACUS Corporate Members

Acuphase Inc.
American Coating Technologies LLC
AMETEK Precitech, Inc.
Berliner Glas KGaA Herbert Kubatz GmbH & Co.
FUJIFILM Electronic Materials U.S.A., Inc.
Gudeng Precision Industrial Co., Ltd.
Halocarbon Products
HamaTech APE GmbH & Co. KG
Hitachi High Technologies America, Inc.
JEOL USA Inc.
Mentor Graphics Corp.
Molecular Imprints, Inc.
Panavision Federal Systems, LLC
Profilocolore Srl
Raytheon ELCAN Optical Technologies
XYALIS

Industry Briefs

Despite 38% Sales Decline, DRAM Expected to Remain Largest IC Market

IC Insights recently released its Mid-Year Update to The McClean Report 2019. It included ranking of the 33 largest IC product categories based on their expected sales and unit shipment volumes for 2019, defined by the World Semiconductor Trade Statistics (WSTS) organization. Despite a 38% sales decline expected this year, the DRAM market is forecast to remain the largest of all IC product categories in 2019 with sales reaching \$62.0 billion, down from \$99.4 billion in 2018. The DRAM market should account for 17% of total IC sales in 2019 compared to 23.6% in 2018. The NAND flash market is forecast to slip from second to third position in the ranking this year with total sales falling 32% to \$40.6 billion. Together, the DRAM and NAND flash memories are forecast to account for 29% of the total \$357.7 billion IC market in this year, compared to 38% of the total IC market in 2018. Over the past decade, DRAM typically accounted for 14-16% of IC sales and NAND flash memory about 11-12%, but tight supplies caused average selling prices to climb, which led to surging sales in both segments in 2017 and 2018. For the first time since the 1990s, DRAM revenues surpassed MPU sales in 2018. http://www.icinsights.com/news/bulletins/Despite-38-Sales-Decline-DRAM-Expected-To-Remain-Largest-IC-Market/

Imec World First to Demonstrate 2 Metal Layer Back-End-of-Line for the 3nm Technology Node

LEUVEN (Belgium), July 8, 2019 — This week, at its technology forum ITF USA 2019, imec, a world-leading research and innovation hub in nanoelectronics, presents a dual-damascene 21nm pitch test vehicle for manufacturing the 3nm logic technology. With this test vehicle, a 30 percent improvement in resistance-capacitance (RC) was obtained compared to previous generations, without impacting reliability. The need for implementing scaling boosters such as self-aligned vias and blocks in 3nm and beyond interconnect technologies has been demonstrated. While the dimensional scaling of traditional front-end technologies is expected to slow down, the back-end-of-line dimensions keep on scaling with ~0.7X to keep up with the required area scaling. For the 3nm logic technology, M2 interconnect layers with metal pitches as tight as 21nm need to be manufactured while preserving the back-end-of-line's performance. This implies a tight control of the RC delay, while maintaining good reliability. To pattern M2, a hybrid lithography approach was proposed, using 193nm immersion-based self-aligned quadrupole patterning (SAQP) for printing the lines and trenches, and extreme ultraviolet lithography (EUVL) for printing the block and via structures. https://www.imec-int.com/en/articles/imec-world-first-to-demonstrate-2-metal-layer-back-end-of-line-for-the-3nm-technology-node

Apple to acquire the majority of Intel's smartphone modem business

Cupertino and Santa Clara, California — Apple and Intel have signed an agreement for Apple to acquire the majority of Intel's smartphone modem business. Approximately 2,200 Intel employees will join Apple, along with intellectual property, equipment and leases. The transaction, valued at \$1 billion, is expected to close in the fourth quarter of 2019, subject to regulatory approvals and other customary conditions, including works council and other relevant consultations in certain jurisdictions. Combining the acquired patents for current and future wireless technology with Apple's existing portfolio, Apple will hold over 17,000 wireless technology patents, ranging from protocols for cellular standards to modem architecture and modem operation. Intel will retain the ability to develop modems for non-smartphone applications, such as PCs, internet-of-things devices and autonomous vehicles. https://www.apple.com/newsroom/2019/07/apple-to-acquire-the-majority-of-intels-smartphone-modem-business/

Join the premier professional organization for mask makers and mask users!

About the BACUS Group

Founded in 1980 by a group of chrome blank users wanting a single voice to interact with suppliers, BACUS has grown to become the largest and most widely known forum for the exchange of technical information of interest to photomask and reticle makers. BACUS joined SPIE in January of 1991 to expand the exchange of information with mask makers around the world.

The group sponsors an informative monthly meeting and newsletter, BACUS News. The BACUS annual Photomask Technology Symposium covers photomask technology, photomask processes, lithography, materials and resists, phase shift masks, inspection and repair, metrology, and quality and manufacturing management.

Individual Membership Benefits include:

- Subscription to BACUS News (monthly)
- Eligibility to hold office on BACUS Steering Committee

spie.org/bacushome

Corporate Membership Benefits include:

- 3-10 Voting Members in the SPIE General Membership, depending on tier level
- Subscription to BACUS News (monthly)
- One online SPIE Journal Subscription
- Listed as a Corporate Member in the BACUS Monthly Newsletter

spie.org/bacushome

CALENDAR

2019

SPIE Photomask Technology + EUV Lithography
15-19 September 2019
Monterey Conference Center and
Monterey Marriott
Monterey, California, USA
www.spie.org/puv

2020

SPIE Advanced Lithography
23-27 February 2020
San Jose Marriott and
San Jose Convention Center
San Jose, California, USA

Photomask Japan
April 2020
Japan

The 36th European Mask and Lithography Conference, EMLC 2020
June 2020
Germany

SPIE is the international society for optics and photonics, an educational not-for-profit organization founded in 1955 to advance light-based science, engineering, and technology. The Society serves nearly 264,000 constituents from 166 countries, offering conferences and their published proceedings, continuing education, books, journals, and the SPIE Digital Library in support of interdisciplinary information exchange, professional networking, and patent precedent. SPIE provided more than $4 million in support of education and outreach programs in 2018. **spie.org**

SPIE.
International Headquarters
P.O. Box 10, Bellingham, WA 98227-0010 USA
Tel: +1 360 676 3290
Fax: +1 360 647 1445
help@spie.org • **spie.org**

Shipping Address
1000 20th St., Bellingham, WA 98225-6705 USA

Managed by SPIE Europe
2 Alexandra Gate, Ffordd Pengam, Cardiff,
CF24 2SA, UK
Tel: +44 29 2089 4747
Fax: +44 29 2089 4750
spieeurope@spieeurope.org • **spieeurope.org**

You are invited to submit events of interest for this calendar. Please send to lindad@spie.org.